Research Article Vol. 32, No. 2 / 15 Jan 2024 / Optics Express 1135
Optics EXPRESS

Joint multi-contrast CT for edge illumination X-ray phase contrast imaging using split Barzilai-Borwein steps

N. Six,[1,2,*] J. Renders,[1,2] J. De Beenhouwer,[1,2] and J. Sijbers[1,2]

[1] *imec-Vision Lab, Department of Physics, University of Antwerp, Belgium*
[2] *DynXlab: Center for 4D Quantitative X-ray Imaging and Analysis, Antwerp, Belgium*
[*] *nathanael.six@uantwerpen.be*

Abstract: Edge illumination (EI) is an X-ray imaging technique that, in addition to conventional absorption contrast, provides refraction and scatter contrast. It relies on an absorption mask in front of the sample that splits the X-ray beam into beamlets, which hits a second absorption mask positioned in front of the detector. The sample mask is then shifted in multiple steps with respect to the detector mask, thereby measuring an illumination curve per detector element. The width, position, and area of this curve estimated with and without the sample in the beam is then compared, which ultimately provides absorption, refraction, and scatter contrast for each detector pixel. From the obtained contrast sinograms, three contrast tomograms can be computed. In summary, conventional EI relies on a two-stage process comprised of a computational and time intensive contrast retrieval process, followed by tomographic reconstruction. In this work, a novel joint reconstruction method is proposed, which utilizes a combined forward model to reconstruct the three contrasts simultaneously, without the need for an intermediate contrast retrieval step. Compared to the state-of-the-art, this approach reduces reconstruction times, as the retrieval step is skipped and allows a much more flexible acquisition scheme, as there is no need to sample a full illumination curve at each projection angle. The proposed method is shown to improve reconstruction quality on subsampled datasets, enabling the reconstruction of three contrasts from single-shot datasets.

1. Introduction

X-ray phase contrast imaging (XPCI) offers complementary contrasts to conventional X-ray absorption: differential phase or refraction contrast, which relates to the refraction of the X-ray beam, and a scatter or dark-field contrast, which relates to scattering caused by sub-voxel micro structures [1]. Compared to absorption contrast, these contrasts have demonstrated the ability to generate higher contrast in soft tissue and enable the visualization of sub-voxel structures, such as those found in composite materials [2]. The applications of XPCI have expanded beyond biomedical studies [3–6] to non-destructive testing [7], materials science [8,9], and security [10,11].

Among the emerging XPCI techniques, edge illumination (EI) is particularly suitable for use with lab-based X-ray sources that have a large focal spot and a polychromatic spectrum [2,12]. In this technique, the phase information can be retrieved by displacing two strongly absorbing masks relative to each other, with the object positioned in between. Conventionally, multiple images at a single view angle are acquired, one for each mask displacement. In every detector element, in every projection, this results in a curve, called the illumination curve. Subsequently, a Gaussian curve is fitted to the illumination curves of each pixel in each projection, both before and after the introduction of a sample. From the two fitted Gaussians, three complementary contrasts are retrieved: absorption, refraction, and scatter. Finally, for each of those contrasts, an

#502542 https://doi.org/10.1364/OE.502542
Journal © 2024 Received 3 Aug 2023; revised 20 Nov 2023; accepted 21 Nov 2023; published 2 Jan 2024

Optics EXPRESS

image is individually reconstructed using filtered backprojection (FBP) or iterative reconstruction techniques.

Unfortunately, EI XPCI requires adequate sampling of the illumination curve at every detector pixel, resulting in long scan times, particularly in computed tomography (CT) imaging. Furthermore, in CT imaging, millions to billions of Gaussian curve fits need to be performed for the contrast retrieval, resulting in a lengthy preprocessing step. Additionally, there is no direct information sharing between the contrasts during reconstruction, limiting their potential synergies.

An alternative to the conventional two-step-approach, in which phase contrast images are reconstructed after phase retrieval, is a one-step-approach, in which phase contrast images are directly reconstructed from the measured X-ray data. In this approach, different contrasts are reconstructed simultaneously, without a separate retrieval step. In grating based Talbot-Lau interferometry (GBI), statistical approaches to one-step joint reconstruction have been proposed [13,14], where a likelihood function is minimized. These approaches were also shown to help reduce scan times as greater freedom in the scanning geometry is allowed [15]. Unfortunately, these techniques cannot be directly applied to EI setups due to the different nature of the measurements between GBI and EI. Both the hardware components as well as the way X-ray refraction affects the measurements, differ. In GBI the resulting changes in interference patterns are compared, while in EI the deflection of the center of the beamlet is considered. Consequently, the forward models developed for GBI are not applicable to EI data.

Recently, an EI reconstruction method was presented in [16] that reconstructs refraction and absorption contrasts separately in a joint reconstruction using line searches. This method achieves a similar flexibility in acquisition setup for EI as reported in [15] for GBI. However, this method does not include scatter reconstructions, which can provide additional information on sample properties [17]. Moreover, no investigation into different suitable solvers for the objective function was performed in [16].

In this work, we propose a novel joint reconstruction method using a full EI forward model without retrieval, enabling the simultaneous reconstruction of all three contrasts. The proposed approach reduces reconstruction times, as the retrieval step is skipped and allows more flexible acquisition schemes. We demonstrate the effectiveness of the proposed method through reconstructions of both simulated and experimental datasets, showing results on single-shot datasets which cannot be reconstructed with the two-step method.

2. Methods

2.1. Edge illumination CT forward model

In EI imaging, the refraction of the X-rays in the object is quantified by incorporating two gratings, called the sample and detector mask, into the traditional X-ray setup, as depicted in Fig. 1(a). The X-ray beam is split into smaller beamlets by the sample mask, with each beamlet corresponding to a pixel on the detector. These beamlets are partially blocked by the detector mask. By performing a phase stepping procedure, which involves lateral translation of the sample mask relative to the detector mask, the fraction of the beamlet blocked by the detector mask changes. The resulting curve obtained by measuring the intensities as a function of the mask translation is referred to as the illumination curve (IC), shown in Fig. 1(b). The IC is assumed to approximate a Gaussian shape. After the introduction of a sample, three contrasts can be retrieved by measuring the changes in the IC: absorption, refraction, and scatter. The change of area under the IC is a measure of the absorption of the sample, the shift of the peak of the IC measures the refraction of the beamlet by the sample, and the broadening of the IC corresponds to the scatter contrast.

We represent the vectors corresponding to absorption, refraction, and scatter reconstructions as $\boldsymbol{x}_\mu$, $\boldsymbol{x}_\delta$, and $\boldsymbol{x}_\sigma$, respectively, where each vector has dimensions $n \times 1$. To combine these vectors

Optics EXPRESS

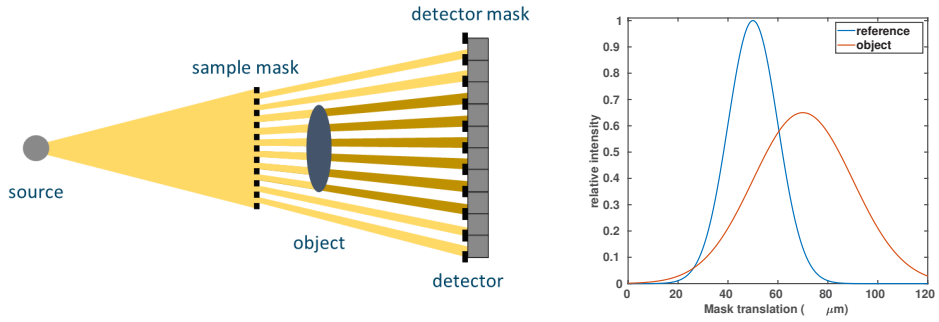

(a) EI imaging set up (b) EI measurements

Fig. 1. (a) overview of an EI setup and (b) flatfield and measured IC.

into a single vector, we define $\boldsymbol{x} \in \mathbb{R}^{3n}$. We assume a Gaussian model for the IC, such that the flatfield intensity $\boldsymbol{p}_0$, as function of the phase step ξ, can be modeled as:

$$\boldsymbol{p}_0(\xi) = a_0 \exp\left(-\frac{(\xi - b_0)^2}{2c_0^2}\right), \tag{1}$$

with a_0, b_0, c_0 the amplitude, mean and standard deviation, respectively. These parameters can be found by phase retrieval, i.e. fitting a Gaussian to the measured flatfield data. In this paper, only a single fit is performed, namely on the mean illumination curve obtained by spatial averaging the intensities of each (phase stepped) flat field. That is, only three parameters are fitted in the preprocessing step.

We now consider models that describe the effects of the introduction of the object $\boldsymbol{x}$ on the beamlets. The absorption of the object, with absorption coefficients $\boldsymbol{x}_\mu$, is modeled by the Beer-Lambert law in X-ray CT as:

$$\boldsymbol{I}(\boldsymbol{x}_\mu) = \boldsymbol{I}_0 \exp\left(-\boldsymbol{A}\boldsymbol{x}_\mu\right), \tag{2}$$

with $\boldsymbol{I}$ the measured intensity, $\boldsymbol{I}_0$ the flatfield intensity, and $\boldsymbol{A} \in \mathbb{R}^{m\times n}$ the discretized X-ray CT projector. In the case of EI, the area under the IC is considered to decrease caused by absorption. Therefore, we employ the same equation as Eq. 2, but where now $\boldsymbol{I}$ and $\boldsymbol{I}_0$ represent the integral of the measured and flatfield IC, respectively. Refraction of the object, which is based on the real part of the refraction index (δ), causes the mean of the measured IC to shift as follows:

$$\boldsymbol{s}(\boldsymbol{x}_\delta) = \boldsymbol{D}\boldsymbol{A}\boldsymbol{x}_\delta, \tag{3}$$

with $\boldsymbol{D} \in \mathbb{R}^{m\times m}$ a discrete differential operator. In what follows, $\boldsymbol{D}$ is the forward differences operator, which has been shown to be a good choice for X-ray phase contrast applications in [18]. Lastly, the dark-field contrast models scattering in the object due to the presence of sub-voxel structures. This shows as broadening of the IC, which we model this as the convolution of the IC with a normal distribution $\mathcal{N}(0, \boldsymbol{A}\boldsymbol{x}_\sigma)$. As such, we obtain the following joint forward projection model, where all operations with vectors are pointwise, except for the matrix-vector products with $\boldsymbol{A}$ and $\boldsymbol{D}$:

$$\boldsymbol{p}(\boldsymbol{x}, \xi) = \exp\left(-\boldsymbol{A}\boldsymbol{x}_\mu\right) \frac{a_0 c_0}{\sqrt{c_0^2 + \boldsymbol{A}\boldsymbol{x}_\sigma}} \exp\left(-\frac{(\xi - b_0 - \boldsymbol{D}\boldsymbol{A}\boldsymbol{x}_\delta)^2}{2\left(c_0^2 + \boldsymbol{A}\boldsymbol{x}_\sigma\right)}\right). \tag{4}$$

Analogously to the construction of $\boldsymbol{x}$, we can still represent $\boldsymbol{p}$ as a vector when multiple phase steps ξ_i per projection angle are considered, by concatenating the different $\boldsymbol{p}(\boldsymbol{x}, \xi_i)$ to create a single vector, which we denote as $\boldsymbol{p}(\boldsymbol{x}, \boldsymbol{\xi})$.

Optics EXPRESS

2.2. Jacobian of the model

Given the forward model in Eq. 4 and some measured data $\boldsymbol{b}$, the reconstruction problem can be seen as a non-linear minimization problem of the following least-squares objective function:

$$\boldsymbol{f}(\boldsymbol{x}) = \frac{1}{2}\,||\boldsymbol{p}(\boldsymbol{x},\boldsymbol{\xi}) - \boldsymbol{b}||_2^2\,, \tag{5}$$

with the reconstruction $\tilde{\boldsymbol{x}}$ being defined as:

$$\tilde{\boldsymbol{x}} = \arg\min_{\boldsymbol{x}} \boldsymbol{f}(\boldsymbol{x}). \tag{6}$$

Non-linear optimization problems of the form of Eq. 6 can be solved in a variety of ways [19]. In this work, versions of gradient descent and quasi-Newton methods were considered. A key advantage of the proposed approach is that, unlike the conventional two-step method of reconstructing after phase retrieval, solving Eq. 6 does not necessitate fully sampled illumination curves for every pixel in each projection. This property was demonstrated in [16] for absorption and refraction contrast.

For the solvers considered in this work, the Jacobian of $\boldsymbol{p}(\boldsymbol{x},\boldsymbol{\xi})$ with respect to $\boldsymbol{x}$ is required. We will denote this Jacobian of $\boldsymbol{p}$ with respect to $\boldsymbol{x}$ in a point $\boldsymbol{x_0}$ as $\boldsymbol{J}_{\boldsymbol{p}}^{\boldsymbol{x}}(\boldsymbol{x_0})$. Given this Jacobian, the gradient of $\boldsymbol{f}$ in Eq. 5 can be written as [19]:

$$\nabla_{\boldsymbol{x}} \boldsymbol{f}|_{\boldsymbol{x}_0} = \boldsymbol{J}_{\boldsymbol{p}}^{\boldsymbol{x}}(\boldsymbol{x}_0)^{\top}(\boldsymbol{p}(\boldsymbol{x_0},\boldsymbol{\xi}) - \boldsymbol{b}). \tag{7}$$

Furthermore, for quasi-Newton methods such as Gauss-Newton and Levenberg-Marquardt [20], the required Hessian matrix of a least-squares problem can be approximated using the Jacobian matrix as:

$$\boldsymbol{H} \approx \boldsymbol{J}^{\top}\boldsymbol{J}. \tag{8}$$

The Jacobian $\boldsymbol{J}_{\boldsymbol{p}}^{\boldsymbol{x}}$ can be seen as a block matrix consisting of the Jacobians with respect to the separate contrasts considered in the model:

$$\boldsymbol{J}_{\boldsymbol{p}}^{\boldsymbol{x}} = \begin{bmatrix} \boldsymbol{J}_{\boldsymbol{p}}^{\boldsymbol{x}_\mu} & \boldsymbol{J}_{\boldsymbol{p}}^{\boldsymbol{x}_\delta} & \boldsymbol{J}_{\boldsymbol{p}}^{\boldsymbol{x}_\sigma} \end{bmatrix} \tag{9}$$

In the case of a single phase step per projection angle, one can calculate the Jacobian of Eq. 4 with respect to the different contrasts as follows:

$$\begin{aligned}
\boldsymbol{J}_{\boldsymbol{p}}^{\boldsymbol{x}_\mu}(\boldsymbol{x}_0) &= -\mathrm{diag}(\boldsymbol{p}(\boldsymbol{x}_0,\xi))\boldsymbol{A} \\
\boldsymbol{J}_{\boldsymbol{p}}^{\boldsymbol{x}_\delta}(\boldsymbol{x}_0) &= \mathrm{diag}\left(\frac{\xi - b_0 - \boldsymbol{D}\boldsymbol{A}\boldsymbol{x}_{0,\delta}}{c_0^2 + \boldsymbol{A}\boldsymbol{x}_{0,\sigma}}\boldsymbol{p}(\boldsymbol{x}_0,\xi)\right)\boldsymbol{D}\boldsymbol{A} \\
\boldsymbol{J}_{\boldsymbol{p}}^{\boldsymbol{x}_\sigma}(\boldsymbol{x}_0) &= \mathrm{diag}\left(\left(\frac{1}{2(c_0^2 + \boldsymbol{A}\boldsymbol{x}_{0,\sigma})}\right)\left(\frac{\left(\xi - b_0 - \boldsymbol{D}\boldsymbol{A}\boldsymbol{x}_{0,\delta}\right)^2}{c_0^2 + \boldsymbol{A}\boldsymbol{x}_{0,\sigma}} - 1\right)\boldsymbol{p}(\boldsymbol{x}_0,\xi)\right)\boldsymbol{A},
\end{aligned} \tag{10}$$

with all operations between vectors being executed pointwise, multiplications between matrices being standard matrix-multiplication and diag the operator transforming a vector into a diagonal matrix. If multiple phase steps per projection angle would be acquired, the resulting Jacobian is the sum of the Jacobians of the form described in Eq. 10 at each of the phase steps. This Jacobian matrix is typically too large to store in memory in real CT use cases, so instead functions are implemented that directly calculate the result of matrix multiplication with this Jacobian, based on the formulas in Eq. 10. All multiplications with the system matrix $\boldsymbol{A}$ or its transpose are performed on the GPU using the ASTRA toolbox [21].

Optics EXPRESS

2.3. Split gradient descent

Gradient descent is a widespread iterative method for solving optimization problems of the form of Eq. 6, where the next iteration is found from the previous as [19]:

$$\boldsymbol{x}^{(k+1)} = \boldsymbol{x}^{(k)} - \alpha^{(k)} \nabla_{\boldsymbol{x}} \boldsymbol{f}|_{\boldsymbol{x}^{(k)}} \,. \tag{11}$$

Analogous to the Jacobian, the gradient of Eq. 5 with respect to $\boldsymbol{x}$ can be divided into partial gradients:

$$\nabla_{\boldsymbol{x}} \boldsymbol{f} = \begin{bmatrix} \nabla_{\boldsymbol{x}_\mu} \boldsymbol{f}^\top & \nabla_{\boldsymbol{x}_\delta} \boldsymbol{f}^\top & \nabla_{\boldsymbol{x}_\sigma} \boldsymbol{f}^\top \end{bmatrix}^\top , \tag{12}$$

For finding a suitable value of $\alpha^{(k)}$ in Eq. 11 multiple options exist [19]. In this paper, we used the Barzilai-Borwein scheme [22] to calculate the step size in iteration k:

$$\alpha^{(k)} = \frac{\left(\boldsymbol{x}^{(k)} - \boldsymbol{x}^{(k-1)}\right) \cdot \left(\nabla_{\boldsymbol{x}} \boldsymbol{f}|_{\boldsymbol{x}^{(k)}} - \nabla_{\boldsymbol{x}} \boldsymbol{f}|_{\boldsymbol{x}^{(k-1)}}\right)}{\left(\nabla_{\boldsymbol{x}} \boldsymbol{f}|_{\boldsymbol{x}^{(k)}} - \nabla_{\boldsymbol{x}} \boldsymbol{f}|_{\boldsymbol{x}^{(k-1)}}\right) \cdot \left(\nabla_{\boldsymbol{x}} \boldsymbol{f}|_{\boldsymbol{x}^{(k)}} - \nabla_{\boldsymbol{x}} \boldsymbol{f}|_{\boldsymbol{x}^{(k-1)}}\right)}. \tag{13}$$

In addition to using this method to find a single step size $\alpha^{(k)}$, we also considered a split gradient descent method where three separate step sizes $\alpha_1^{(k)}, \alpha_2^{(k)}, \alpha_3^{(k)}$ are calculated for the partial gradients shown in Eq. 12. This allows the step size of the three contrasts to vary independently, with the hypothesis being that this would alleviate the need to find scaling parameters between the different contrasts.

3. Results & discussion

To assess the effectiveness of the proposed joint reconstruction method, we conducted evaluations on both simulated and experimental datasets. For the simulated dataset, we employed multiple optimizers and assessed their performance based on two metrics: projection error and mean squared error (MSE) with respect to the ground truth. To ensure a fair comparison, gradient descent with Barzilai-Borwein steps was implemented for use with each of the separate contrasts after phase retrieval, using the same forward operators, $\boldsymbol{A}$ and $\boldsymbol{DA}$, as the joint reconstruction model.

3.1. Simulated data

A simulation experiment was set up to select an appropriate optimization algorithm and to compare the joint reconstructions to the conventional two step workflow of reconstruction after phase retrieval. A phantom was defined on a 2000×2000 pixel grid, with a pixel size of 60 µm. The different ground truth contrast channels of the phantom are shown in Fig. 2. A total of 360 fan beam projection angles were considered, evenly distributed over a 360° range. For each projection angle, five projections were obtained with varying simulated sample mask displacements at $-13.5, -9, 0, 9$ and 13.5 µm, resulting in a total of 1800 fan beam projections The magnification factor was 1.25. The projections were created using the forward model in Eq. 4. To avoid using the same model in both simulation and reconstruction, the projections were computed on a 2000×2000 pixel grid, but reconstructed on a 500×500 pixel grid. It should be noted that, for the purpose of comparing with the conventional workflow, the model in Eq. 4 simulates Gaussians, which benefits the phase retrieval process.

In the first experiment, we compared the performance of different optimizers for the joint reconstruction approach, on the full dataset. The same reconstructions were performed with gradient descent with Barzilai-Borwein steps (GD-BB) [22], split gradient descent with Barzilai-Borwein steps (split-GD-BB), Gauss-Newton-Krylov (GNK) [19] and Levenberg-Marquardt-Krylov (LMK) [20]. Each contrast channel in the joint model can be scaled individually, which corresponds to changing the unit of the reconstructed values. These different potential scaling

Optics EXPRESS

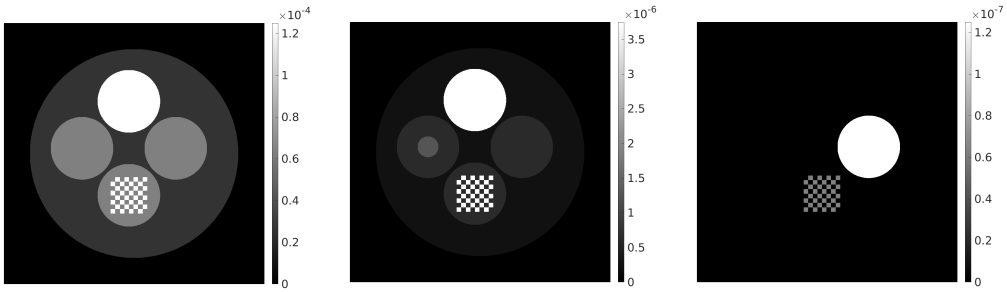

(a) Absorption (b) Refraction (c) Scatter

Fig. 2. Different contrast channels, (a) absorption, (b) refraction and (c) scatter, of the ground truth phantom used for the simulation experiments.

factors can have an impact on convergence speed and reconstruction quality. Therefore, the three different contrasts were each multiplied with scaling factors in $\{10^{-4}, 10^{-3}, 10^{-2}, 10^{-1}, 1, 10\}$, resulting in $6^3 = 216$ different reconstructions for each method. The GD-BB and split-GD-BB were run for 500 iterations, GNK and LMK were run for 50 outer iterations with 10 inner Krylov iterations in each outer iteration. Two measures of the error are considered: projection error and mean squared error (MSE) with respect to the ground truth. For the projection error the reconstructed images are projected again using Eq. 4 and MSE with the measured data is calculated. For the MSE with respect to the ground truth, the MSE of the reconstruction with respect to each ground truth contrast channel is calculated separately. The box plots in Fig. 3 illustrate the minimum achieved projection error and ground truth MSE. It can be observed that the reconstruction quality varies significantly depending on the scaling factors employed, except in the case of split-GD-BB. This can be attributed to the fact that split-GD-BB computes different step sizes for each contrast, making it less sensitive to relative scaling. Notably, the minimum achieved error in an outlier for GD-BB, GNK, and LMK, different for each one, is slightly lower compared to the split-GD-BB error. However, split-GD-BB offers the advantage of not requiring the determination of optimal parameters. The determination of scaling factors severely limits the practical application of the other optimizers for real reconstruction problems. Even when found, the GD-BB, GNK and LMK methods with optimal parameters do not output noticeably improved reconstructions over split-GD-BB without optimal parameters. Therefore, in the following experiments, only split-GD-BB was used as the optimizer for the proposed the joint reconstruction method.

Next, the reconstruction quality and convergence speed was compared between the joint reconstruction method with split-GD-BB optimizer and the two-step method with GD-BB optimizer. In both cases three step sizes were calculated with the BB formula for a single update of each contrast. Of both methods, 2000 iterations were performed and timed. For the two-step method, Gaussian curves were first fitted to each of the $360 \times 500 = 180.000$ ICs, using MATLAB's built-in LSQCURVEFIT function with trust region approach. The plots showing different errors, projection error and ground truth MSE, as function of number of iterations are shown in Fig. 4. The reconstructions after 2000 iterations are shown in Fig. 5. The total time and time per iteration are shown in Table. 1. From these figures, it is clear that the differences on the full dataset between the two reconstruction methods are minimal. The ground truth phantom is faithfully reconstructed, with the exception of some light streaking artefacts, for both methods. Comparing the difference images with the ground truth (not shown here), reveals that there are some additional weak artefacts at the interfaces between the materials, again of the same magnitude for both methods, which is likely due to the downsampling of the projection data.

Optics EXPRESS

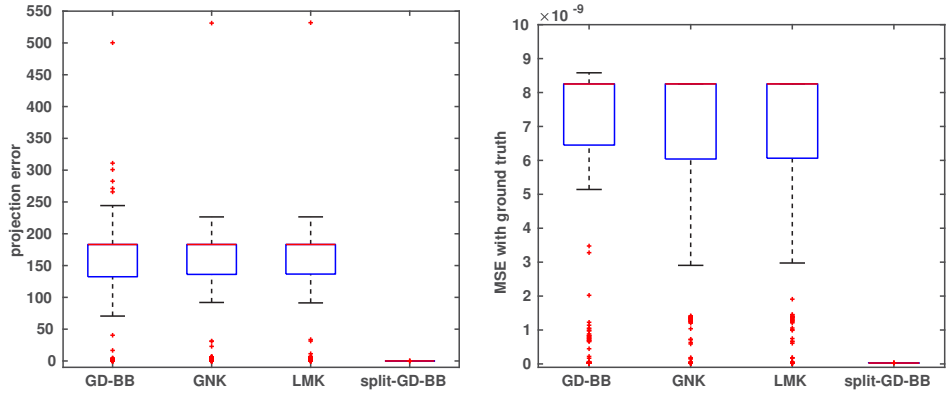

(a) Boxplot of projection error

(b) Boxplot of MSE with respect to the ground truth

Fig. 3. Box plots showing the variation, by using different relative scaling of the contrasts, in minimally achieved projection error (a) and MSE with respect to the ground truth (b) for different optimizers of the EI objective function.

The joint reconstruction method reaches a lower projection error although differences in ground truth MSE are negligible. As both methods converge to the same reconstructions, the proposed joint reconstruction method has the benefit of providing this reconstruction faster, as it does not require a lengthy phase retrieval preprocessing step.

Table 1. Table of total times and time per iteration of the phase retrieval, reconstruction after phase retrieval and joint reconstruction on the full dataset with five phase steps. Time per iteration for the phase retrieval algorithm is the time per IC. Reconstruction algorithms were run for 2000 iterations, phase retrieval was performed on $500 \times 360 = 180000$ IC's.

Algorithm	Time per iteration	Total time
Phase retrieval	0.0142 s	2560 s
Reconstruction after retrieval	0.0595 s	119 s
Joint reconstruction	0.111 s	221 s

Additionally, the stability of the reconstructed values when noise is present in the projection data was investigated. The above experiment was repeated after Poisson noise was added to the projection data, for a flatfield intensity of 100000 photon counts per detector element. Twenty independent noise realisations were considered and bias and standard deviation maps for both methods and for each contrast were calculated. For absorption and refraction both methods performed virtually identically. The bias and standard deviation maps for scatter are shown in Fig. 6. It can be seen that the standard deviation of the proposed method for scatter is significantly lower than that of the conventional two-step method. A possible explanation is that errors due to noise made in the IC fitting procedure propagate through, leading to less predictable reconstructions for the two-step method.

Lastly, the method was tested as a single-shot reconstruction algorithm. For each projection angle, a single projection at one mask displacement was acquired (i.e., no phase stepping at any projection angle). When moving to the next projection angle, the sample mask was stepped only once, to the next displacement in the full range of phase steps: $-13.5 - 9, 0, 9$ and $13.5\,\mu$m, returning to $-13.5\,\mu$m at the end of the list. This sampling method is similar to the cycloidal CT presented in [23], where the sample undergoes a lateral displacement following each rotational

Optics EXPRESS

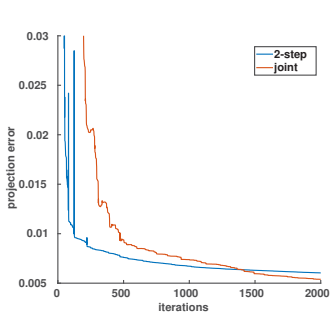

(a) Projection error.

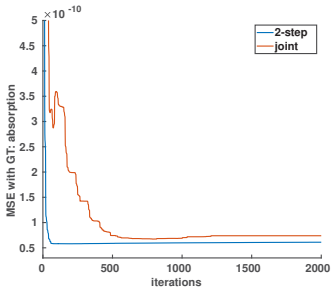

(b) MSE with respect to ground truth absorption.

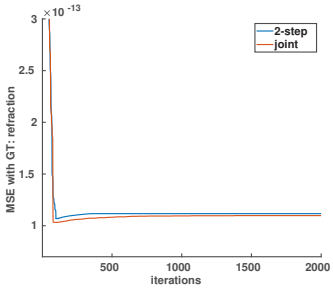

(c) MSE with respect to ground truth refraction.

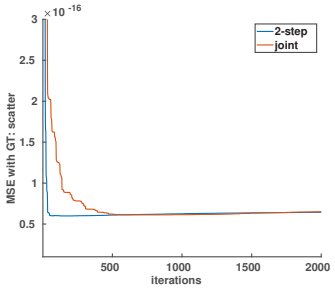

(d) MSE with respect to ground truth scatter.

Fig. 4. Plots of reconstruction quality as a function of the number of iterations for the simulated dataset, comparing the two-step method with GD-BB optimization and the joint reconstruction method with split-GD-BB optimization. Two error measures are shown: (a) projection error, measuring how well the simulated projection of the reconstruction fits with the measured data and (b-d) MSE with respect to the ground truth for each contrast channel separately.

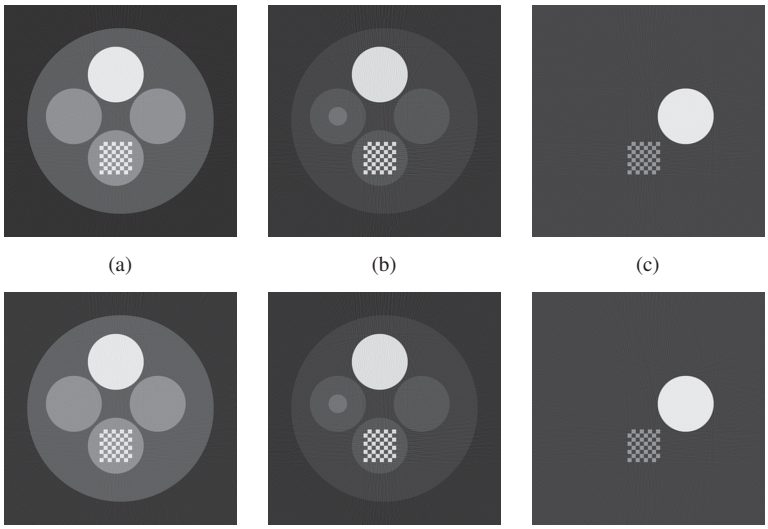

(a) (b) (c)

(d) (e) (f)

Fig. 5. Reconstructions of the simulated dataset with 5 phase steps per projection. (a-c) two-step reconstruction method with GD-BB and (d-f) joint reconstruction method with split-GD-BB. Different contrast per column, left to right: absorption, refraction, scatter.

Optics EXPRESS

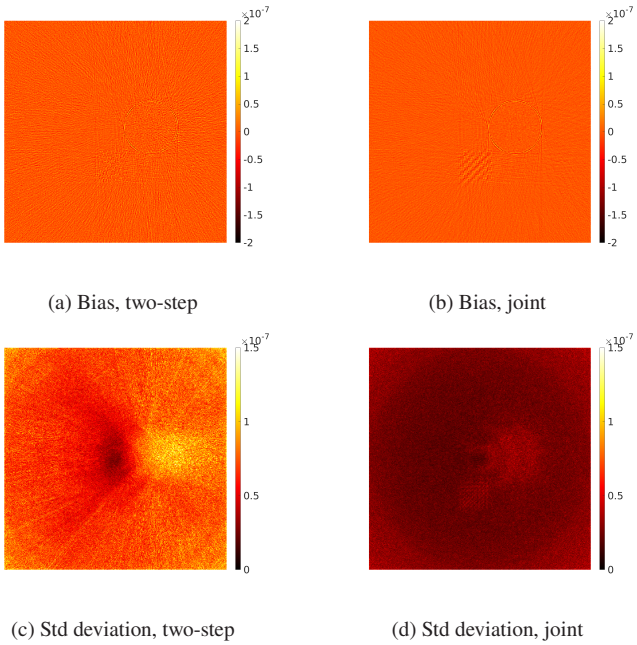

(a) Bias, two-step (b) Bias, joint

(c) Std deviation, two-step (d) Std deviation, joint

Fig. 6. Bias (a-b) and standard deviation (c-d) maps of the scatter contrast for the simulated dataset from twenty repeated noise experiments.

step. The simulated dataset acquired this way for 360 uniformly distributed projections is a subset of the simulated dataset described before, with only 20% of the data available.

For the joint reconstruction method, the above described projection data can be reconstructed directly. However, for the conventional two-step method, this is not possible, as no Gaussian fitting can be performed to a single point in each projection pixel. To allow for a comparison with the two-step method from the same dataset, the available data was interpolated to recreate 5 phase steps per projection. The data available at each mask displacement was used to fill in the missing projection angles at that displacement, using cubic interpolation. The two-step method was subsequently performed on this interpolated dataset. The joint reconstruction method was performed on both the original single-shot data and the interpolated dataset. The same single-shot methodology was also followed on a subset of the simulated data where only half of projection angles are taken.

The error measurements of this experiment are shown in Fig. 7 and reconstructions after 2000 iterations for each method are shown in Fig. 8. From the plots in Fig. 7, it can be observed that the proposed method on the non-interpolated data converges to a much lower projection error than the two-step method on the interpolated dataset, while the proposed method on the interpolated data converges to a slightly higher projection error. Furthermore, the different ground truth MSE plots show that both methods exhibits semi-convergent behaviour when performed on the interpolated data. However, the joint reconstructions on the single-shot data without interpolation do not show this semi-convergent behaviour. Although the methods on the interpolated data have a low MSE with respect to the ground truth after a low amount of iterations, the reconstruction here is extremely blurry and still has a high projection error. From the qualitative comparison in Fig. 8, it can be seen that both methods suffer from artefacts due to the subsampling. However, the reconstructions on interpolated data are unable to reconstruct the fine details, as they are lost in rotational blurring from the interpolation, which is especially visible in the checkerboard part of the phantom. In the reconstructions, a slight improvement of the reconstruction quality of the

Optics EXPRESS

scatter contrast can be observed for the joint reconstruction on interpolated data, compared to the two-step method. The proposed joint reconstruction method on the data without interpolation still reconstructs most of the interior faithfully. When the number of single-shot projections is halved, it can be observed again in Fig. 9 that the quality of the reconstructions with the proposed method degrades much less severely than for the ones with the two-step method on interpolated data. This is to be expected, as the lower the number of single-shot projections, the more error is introduced by the interpolation method. In summary, the proposed method provides more accurate reconstructions without the need of a preprocessing step consisting of interpolation and phase retrieval.

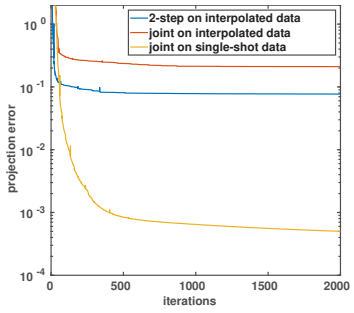

(a) Projection error.

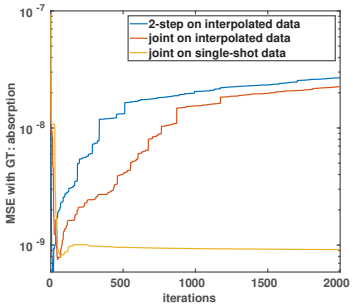

(b) MSE with respect to ground truth absorption.

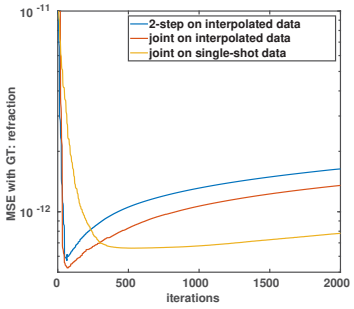

(c) MSE with respect to ground truth refraction.

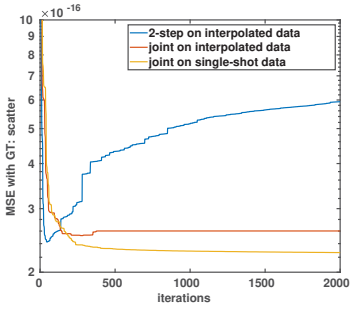

(d) MSE with respect to ground truth scatter.

Fig. 7. Plots of reconstruction quality as function of number of iterations for the simulated dataset with one phase step per projection, comparing the two-step method with GD-BB optimization on the interpolated data and the joint reconstruction method with split-GD-BB optimization on both the interpolated data and the single shot data: (a) projection error (b-d) MSE with respect to the ground truth, for each contrast channel separately.

3.2. *Experimental dataset: fiber polymer*

To further evaluate the performance of the joint reconstruction method and to confirm the conclusions from the simulation results of section 3.1, reconstructions from an experimental dataset were compared. The data consists of the central slice of a cone beam edge illumination dataset, acquired at the Advanced X-Ray Imaging Group, University College London. The imaged object was a fiber polymer block with fiber bundles woven in two orthogonal directions, held in place by plastic straws. Over a 360° range, 6250 projections were acquired, from 1250 uniformly spaced angles, with 5 phase steps per projection angle. From this fully sampled dataset, two reconstruction experiments were set up. First, reconstructions were made from all available data using both the conventional two-step method as well as the proposed joint reconstruction

Optics EXPRESS

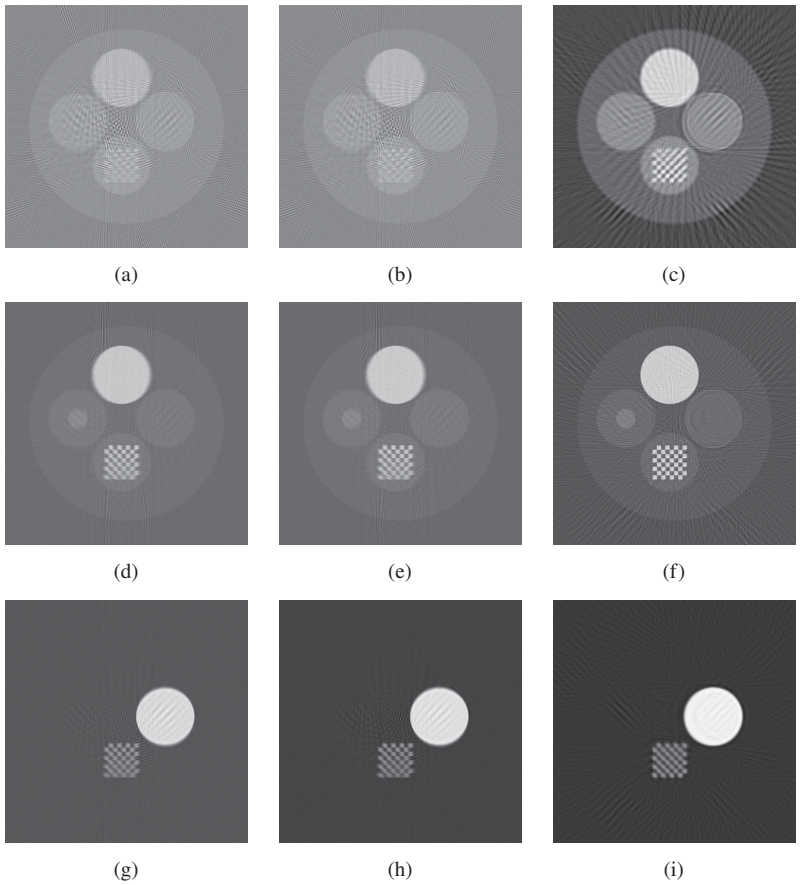

Fig. 8. Reconstructions of the simulated single-shot data with 360 projections: (a-c) absorption, (d-f) refraction, (g-i) scatter. Columns from left to right: two-step method on the interpolated single-shot data, joint reconstruction split-GD-BB on interpolated single-shot data, joint reconstruction split-GD-BB on single-shot data.

method. As no ground truth was available for this dataset, only the projection error was computed for this experiment. Next, subsets of the data were taken to simulate a single-shot dataset of the same object. Both the full range with 1250 and a subsampled range with 500 projections were considered. For this experiment, the MSE with respect to the reconstruction found in the first experiment is calculated, considering this as the best guess for the ground truth object. As undersampling artefacts in the background would be the main contributor to this MSE, the MSE with respect to the ground truth is calculated only in the region where the object is present. For the two-step method, reconstructions were again computed using GD-BB on the retrieved sinograms. As the simulation results in section 3.1 suggest that split-GD-BB performs well and has less parameters that need to be tuned, only this optimizer was used for the joint reconstruction method for the experimental data. For both methods the optimizer was run for 500 iterations.

In Fig. 10, the evolution of the projection error over iterations is shown for the fully sampled dataset. The joint method reaches a lower projection error compared to the two-step method. The reconstructions made with the joint reconstruction method are therefore more faithful to the projection data. Erratic behaviour can be observed in the projection error curves, however, this is known behaviour of gradient descent when using Barzilai-Borwein steps [24]. In Figs. 11(a)–11(f)

Optics EXPRESS

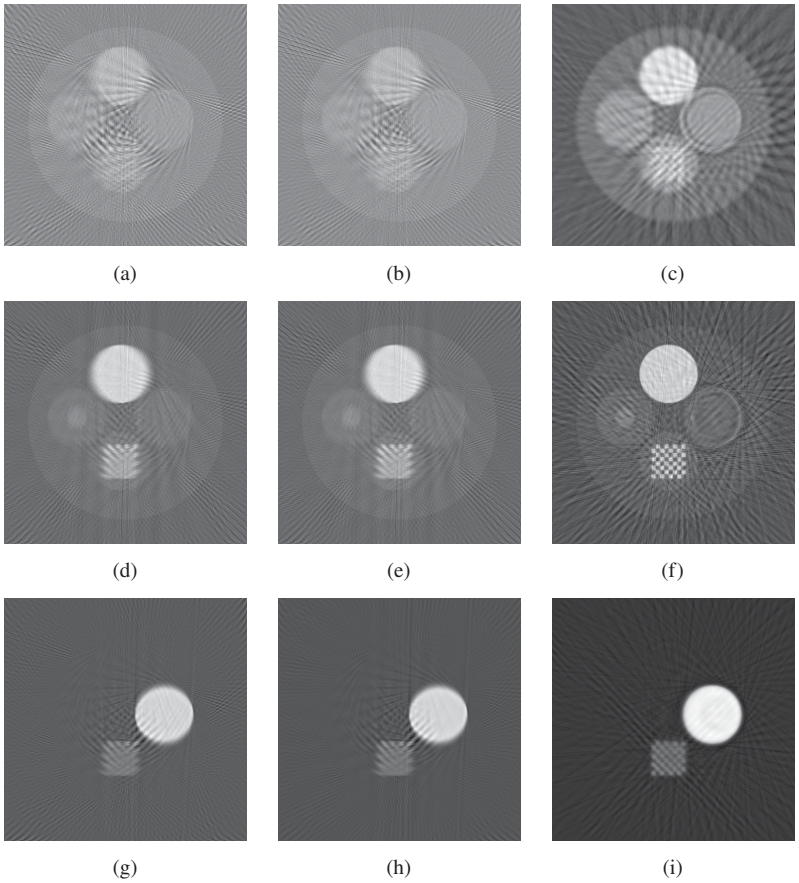

Fig. 9. Reconstructions of the simulated single-shot data with 180 projections: (a-c) absorption, (d-f) refraction, (g-i) scatter. Columns from left to right: two-step method on the interpolated single-shot data, joint reconstruction split-GD-BB on interpolated single-shot data, joint reconstruction split-GD-BB on single-shot data.

the reconstructions after 500 iterations are shown. The reconstructions are again visually very similar on the full dataset, which is in line with the simulation results.

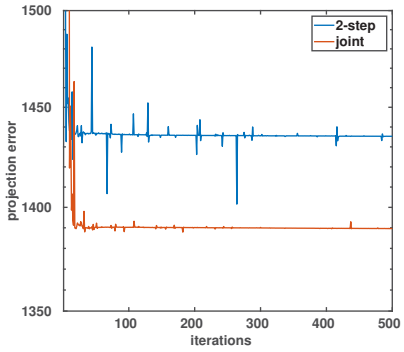

Fig. 10. Plot of projection error as function of iterations for the experimental dataset, comparing the two-step and joint reconstruction methods.

Optics EXPRESS

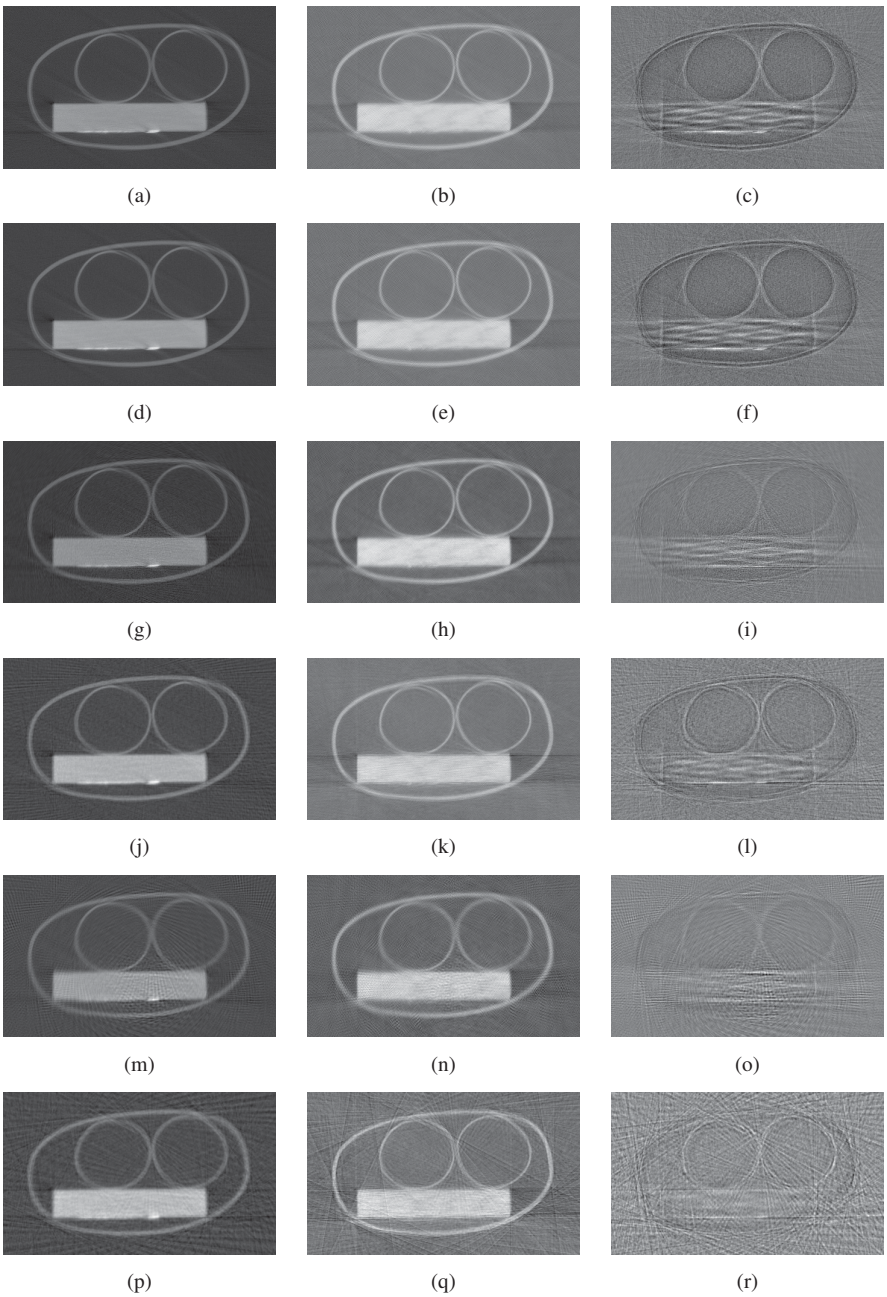

Fig. 11. Cropped reconstructions of the fiber polymer block. (a-c) two-step method of the full dataset, (d-f) joint reconstruction method on the full dataset, (g-i) two-step method on 1250 single-shot projections, (j-l) joint reconstruction method on 1250 single-shot projections, (m-o) two-step method on 500 single-shot projections, (p-r) joint reconstruction method on 500 single-shot projections. Columns from left to right: absorption, refraction, and scatter contrasts.

Next, the results of the single-shot experiment were compared. In Fig. 12, the evolution of the MSE with respect to the 'ground truth' reconstruction is shown and in Figs. 11(g)–11(r) the reconstructions are qualitatively compared. The joint method reaches a lower MSE with respect

Optics EXPRESS

to the ground truth reconstruction compared to the two-step method on interpolated data in almost all cases. There is one exception: in refraction contrast with all 1250 projections, the measured error for the two-step method is slightly lower than the joint reconstruction method. In general, this is again in line with the simulation results, showing that the joint reconstruction method is able to compute accurate reconstructions from single-shot datasets. In Fig. 11(g)–11(r), the reconstructions can be compared. The reconstructions with the joint method on the single-shot data are sharper than the two-step reconstructions on the interpolated data. The reconstructions of the interpolated data tend to have less background artefacts, as everything gets smoothed out slightly due to the rotational blurring. It is important to note that this blurring effect is not due to the two-step method, but inherent to the interpolation. Therefore, if the blurred reconstruction would qualitatively be preferred, the joint reconstruction method can also be employed on the interpolated dataset. This would result in similar reconstructions, without the need for a preprocessing step, as in the full data case studied before.

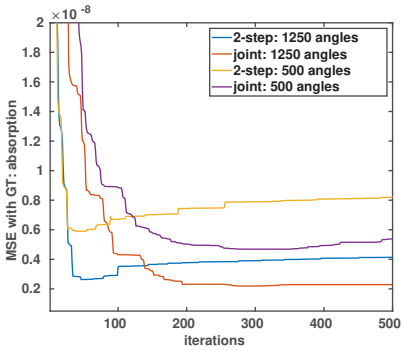

(a) MSE with respect to ground truth absorption.

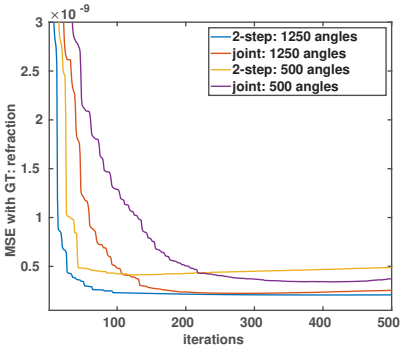

(b) MSE with respect to ground truth refraction.

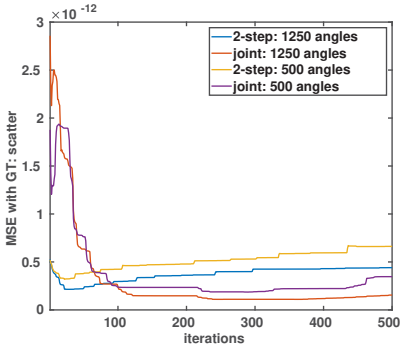

(c) MSE with respect to ground truth scatter.

(d) Mask for MSE.

Fig. 12. (a-c) Plots of reconstruction quality as function of number of iterations for the experimental dataset with one phase step per projection, comparing the two-step method and the joint reconstruction method MSE with respect to the ground truth, for each contrast channel separately. The results on both 1250 and 500 projection angles are compared. (d) ROI where the MSE is calculated.

Future work building upon the proposed work can be envisioned in multiple fronts. To use the greater freedom in acquisition schemes, one could investigate ideal sampling schemes with varying rotational, dithering [23] and phase steps, as well as varying exposure times, using the proposed method. In modeling, more accurate physics models can be investigated, extending the forward model to include for example effects of polychromatic sources and directionality of

Optics EXPRESS

scatter. Other choices for the differential operator for refraction contrast can also be considered. Furthermore, regularisation terms for the different contrast channels, as well as joint regularisation using data from multiple contrast channels at once could be considered. Additionally, the forward model proposed here can also be used as the model for iterative statistical reconstruction methods, by adjusting the objective function according to a chosen noise model.

4. Conclusion

Conventional EI-based phase contrast reconstruction employs a two-step procedure: the fitting of a Gaussian function to the IC of each detector pixel to retrieve absorption, refraction, and scatter contrast, followed by the reconstruction of each of these contrasts. Significant drawbacks of this approach are the lengthy preprocessing of the data required before reconstruction and the necessity for complete sampling of each IC at every projection angle. In our paper, we introduced a joint reconstruction method capable of simultaneous reconstruction of all three contrasts: absorption, refraction, and scatter. We furthermore investigated different optimizer choices and concluded that gradient descent with a split Barzilai-Borwein scheme performed the best in terms of convergence speed and reconstruction quality with little scaling of the objective function needed. We showed that the proposed method reconstructs equally reliably as the state-of-the-art two-step procedure when using the same datasets, but without the need of performing phase retrieval. Furthermore, the method allows for more freedom in acquisition schemes, as we showed that images can also be reconstructed from single-shot datasets that cannot be reconstructed with the two-step procedure without additional interpolation.

Funding. Interreg Vlaanderen-Nederland (Smart*Light (0386)); Fonds Wetenschappelijk Onderzoek (11D8319N, 1SA2920N, G090020N, G094320N, S003421N).

Acknowledgments. The authors would like to thank Dr. S. Savvidis and Dr. A. Olivo for their help and support in providing the experimental dataset for this research. Portions of this work were presented at the SPIE optics and photonics conference in 2022, "Joint reconstruction of attenuation, refraction and dark field X-ray phase contrasts using split Barzilai-Borwein steps" [25].

Disclosures. The authors declare no conflicts of interest.

Data availability. Data underlying the results presented in this paper are not publicly available at this time, but may be obtained from the authors upon reasonable request.

References

1. M. Endrizzi, "X-ray phase-contrast imaging," Nucl. Instrum. Methods Phys. Res., Sect. A **878**, 88–98 (2018).
2. A. Olivo, "Edge-illumination X-ray phase-contrast imaging," J. Phys.: Condens. Matter **33**(36), 363002 (2021).
3. A. Momose, T. Takeda, Y. Itai, *et al.*, "Phase-contrast X-ray computed tomography for observing biological soft tissues," Nat. Med. **2**(4), 473–475 (1996).
4. F. Arfelli, M. Assante, V. Bonvicini, *et al.*, "Low-dose phase contrast X-ray medical imaging," Phys. Med. Biol. **43**(10), 2845–2852 (1998).
5. M. Marenzana, C. K. Hagen, P. D. N. Borges, *et al.*, "Synchrotron-and laboratory-based X-ray phase-contrast imaging for imaging mouse articular cartilage in the absence of radiopaque contrast agents," Phys. Med. Biol. **372**(2010), 20130127 (2014).
6. L. Massimi, T. Suaris, C. K. Hagen, *et al.*, "Volumetric High-Resolution X-Ray Phase-Contrast Virtual Histology of Breast Specimens With a Compact Laboratory System," IEEE Trans. Med. Imaging **41**(5), 1188–1195 (2022).
7. D. Shoukroun, L. Massimi, M. Endrizzi, *et al.*, "Edge illumination X-ray phase contrast imaging for impact damage detection in CFRP," Mater. Today Commun. **31**, 103279 (2022).
8. Z. Hu, P. Thomas, A. Snigirev, *et al.*, "Phase-mapping of periodically domain-inverted LiNbO3 with coherent X-rays," Nature **392**(6677), 690–693 (1998).
9. V. Revol, I. Jerjen, C. Kottler, *et al.*, "Sub-pixel porosity revealed by X-ray scatter dark field imaging," J. Appl. Phys. **110**(4), 044912 (2011).
10. A. Olivo, D. Chana, and R. Speller, "A preliminary investigation of the potential of phase contrast X-ray imaging in the field of homeland security," J. Phys. D: Appl. Phys. **41**(22), 225503 (2008).
11. A. Olivo, K. Ignatyev, P. Munro, *et al.*, "Design and realization of a coded-aperture based X-ray phase contrast imaging for homeland security applications," Nucl. Instrum. Methods Phys. Res., Sect. A **610**(2), 604–614 (2009).
12. A. Zamir, C. Hagen, P. C. Diemoz, *et al.*, "Recent advances in edge illumination X-ray phase-contrast tomography," J. Med. Imag. **4**(04), 1 (2017).

Optics EXPRESS

13. A. Ritter, F. Bayer, J. Durst, *et al.*, "Simultaneous maximum-likelihood reconstruction for x-ray grating based phase-contrast tomography avoiding intermediate phase retrieval," arXiv, arXiv:1307.7912 (2013).
14. B. Brendel, M. von Teuffenbach, P. B. Noël, *et al.*, "Penalized maximum likelihood reconstruction for x-ray differential phase-contrast tomography," Med. Phys. **43**(1), 188–194 (2015).
15. M. von Teuffenbach, T. Koehler, A. Fehringer, *et al.*, "Grating-based phase-contrast and dark-field computed tomography: a single-shot method," Sci. Rep. **7**(1), 1–8 (2017).
16. Y. Chen, H. Guan, C. K. Hagen, *et al.*, "Single-shot edge illumination X-ray phase-contrast tomography enabled by joint image reconstruction," Opt. Lett. **42**(3), 619–622 (2017).
17. A. Doherty, S. Savidis, A. Astolfo, *et al.*, "X-ray dark-field tomography using edge-illumination," Proc. SPIE **12242**, 8 (2022).
18. N. Schenkels, J. Sijbers, W. van Aarle, *et al.*, "A generalized bidiagonal-tikhonov method applied to differential phase contrast tomography," arXiv, arXiv:1510.03233 (2015).
19. J. Nocedal and S. J. Wright, *Numerical Optimization*, 2nd ed (Springer, 2006).
20. K. Levenberg, "A method for the solution of certain non-linear problems in least squares," Q. Appl. Math. **2**, 164–168 (1944).
21. W. van Aarle, W. J. Palenstijn, J. Cant, *et al.*, "Fast and flexible X-ray tomography using the ASTRA toolbox," Opt. Express **24**(22), 25129–25147 (2016).
22. J. Barzilai and J. M. Borwein, "Two-point step size gradient methods," IMA J. Numer. Anal. **8**(1), 141–148 (1988).
23. C. K. Hagen, F. A. Vittoria, O. R. i Morgó, *et al.*, "Cycloidal computed tomography," Phys. Rev. Appl. **14**(1), 014069 (2020).
24. E. G. Birgin, J. M. Martínez, and M. Raydan, "Spectral projected gradient methods: review and perspectives," J. Stat. Soft. **60**(3), 1–21 (2014).
25. N. Six, J. Renders, J. De Beenhouwer, *et al.*, "Joint reconstruction of attenuation, refraction and dark field x-ray phase contrasts using split barzilai-borwein steps," Proc. SPIE **12242**, 22 (2022).